Available online at www.sciencedirect.com
SCIENCE DIRECT®
Icarus 171 (2004) 284–294
ICARUS
www.elsevier.com/locate/icarus

Elastic dislocation modeling of wrinkle ridges on Mars

Thomas R. Watters

Center for Earth and Planetary Studies, National Air and Space Museum, Smithsonian Institution, Washington, DC 20560-0315, USA

Received 26 February 2004; revised 25 May 2004

Available online 18 August 2004

Abstract

Wrinkle ridges are one of the most common landforms on Mars. Although it is generally agreed that they are compressional tectonic features formed by folding and thrust faulting, there is no consensus on the number of faults involved, the geometry of the faults, or the maximum fault depth. The topography of martian wrinkle ridges in Solis Planum and Lunae Planum has been studied using MOLA data. As determined in previous studies, the topography shows that most wrinkle ridges are a composite of two landforms, a broad low relief arch and a superimposed ridge. Constrained by MOLA topographic profiles, the geometry and parameters of the faults associated with wrinkle ridges have been modeled. The best fits are obtained with a blind listric thrust fault that flattens into a décollement. The listric fault geometry is approximated by a series of linear connecting segments with varying dips. The major morphologic elements of wrinkle ridges can be matched by varying the displacement on the different fault segments. Modeling of large-scale wrinkle ridges indicates that the maximum depth of faulting or depth to the décollement is about 4.5 km. This may correspond to the depth of the contact between the ridged plains volcanic sequence and the underlying megabreccia. The results suggest that wrinkle ridge thrust faults are shallow-rooted and reflect thin-skinned deformation.
Published by Elsevier Inc.

Keywords: Mars, tectonics; Mars, surface

1. Introduction

The first observations of wrinkle ridges were made on lunar mare surfaces using Earth-based telescopes. Exploration of the terrestrial planets has revealed analogous landforms on smooth plains of Mercury, Venus, and Mars, and analogous structures have been identified on Earth. The distinctive morphology of wrinkle ridges, first characterized in studies of mare ridges, consists of a broad, low relief arch and a narrow, superimposed ridge (e.g., Strom, 1972; Bryan, 1973; Maxwell et al., 1975). The lack of high resolution topographic data for the Moon, Mercury, Venus, and, until recently, Mars has made detailed morphologic studies of wrinkle ridges difficult. Martian wrinkle ridges have been studied using photoclinometrically derived topography from Viking Orbiter images (Golombek et al., 1991; Watters and Robinson, 1997). Ambiguities in this topography made it difficult to establish if elevation offsets from one side of the ridge to the other (Golombek et al., 1991; Plescia, 1991, 1993) are key morphologic elements or artifacts of regional slope and other factors (Watters and Robinson, 1997). Even though the topography of martian wrinkle ridges can now be characterized with much greater accuracy using Mars Orbiter Laser Altimetry (MOLA) data (Smith et al., 1999, 2001; Zuber et al., 2000), the debate continues as to the existence, nature, and importance of elevation offsets (Watters and Robinson, 2000; Golombek et al., 2001; Okubo and Schultz, 2001; Watters, 2001).

Since the first observations of wrinkle ridges on lunar mare surfaces, their origin has been debated. This is reflected by the variety of kinematic models that have been proposed for their origin (see Schultz, 2000). With few exceptions, it is generally agreed that wrinkle ridges are the result of compressional tectonism, reflecting folding and thrust faulting (Bryan, 1973; Howard and Muehlberger, 1973; Muehlberger, 1974; Maxwell et al., 1975; Lucchitta, 1976, 1977; Maxwell and Phillips, 1978; Sharpton and Head, 1982, 1988). Although a compressional origin is supported

E-mail address: twatters@nasm.si.edu.

0019-1035/$ – see front matter Published by Elsevier Inc.
doi:10.1016/j.icarus.2004.05.024

by studies of terrestrial analogs (Plescia and Golombek, 1986; Watters, 1988; Schultz, 2000), there is no consensus on the geometry and number of faults or the importance of folding (Golombek et al., 1991, 2001; Tanaka et al., 1991; Watters, 1991, 1993; Watters and Robinson, 1997; Schultz, 2000). Another contentious area is the depth of faulting, specifically if wrinkle ridges are an expression of thick- or thin-skinned deformation (Zuber and Aist, 1990; Watters, 1991, 1993; Tanaka et al., 1991; Zuber, 1995; Watters and Robinson, 1997; Golombek et al., 2001; Montesi and Zuber, 2003a, 2003b).

Wrinkle ridges in Solis and Lunae Plana have been examined using MOLA topographic data. These data are used to constrain elastic dislocation modeling of wrinkle ridge thrust faults in an effort to determine the fault geometry and maximum depth of faulting. Thick- versus thin-skinned deformation and the influence of mechanical properties are also discussed.

2. Topography

The MOLA instrument onboard the Mars Global Surveyor (MGS) has provided global high resolution topographic data for Mars (Smith et al., 1998, 1999, 2001; Zuber et al., 1992, 2000). These data have a maximum vertical resolution of about 30 cm and along-track spatial resolution of 300 to 400 m (Smith et al., 1998, 2001). The relief and morphology of wrinkle ridges were examined by generating digital elevation models (DEMs) from MOLA orbital profiles. These data were gridded at a spatial resolution of 300 m/pixel and then interpolated using kriging. Crossover statistics were collected for each MOLA orbital profile in the DEM area (see Neumann et al., 2001) to determine if a given orbital profile is offset relative to others in the DEM area. If an orbital profile is significantly offset, it was not included in the DEM. Profiles across the wrinkle ridges were then generated in several locations (usually 3 to 4) to determine the average morphology of a ridge segment.

2.1. Lunae Planum

Wrinkle ridges in Lunae Planum generally trend north–south and are regularly spaced at a distance averaging 20 to 35 km (Watters, 1991) (Fig. 1). The ridged plains of Lunae Planum are on a plateau that slopes downward to the east and is bordered to the north by Kasei Valles and to the south by Valles Marineris (Fig. 1). Profiles across wrinkle ridges generated using MOLA data clearly reflect the most common morphologic elements, a prominent ridge superimposed on the flank of a broad, low relief arch (Fig. 2). The largest wrinkle ridge examined in Lunae Planum (LP1) has a maximum relief of about 250 m (Fig. 2B). The superimposed ridge has a maximum width of about 9 km and the entire structure is roughly 30 km wide. Another prominent wrinkle ridge to the east (LP2), has the same morphologic elements as LP1, but has about half the maximum relief (~ 130 m) and width

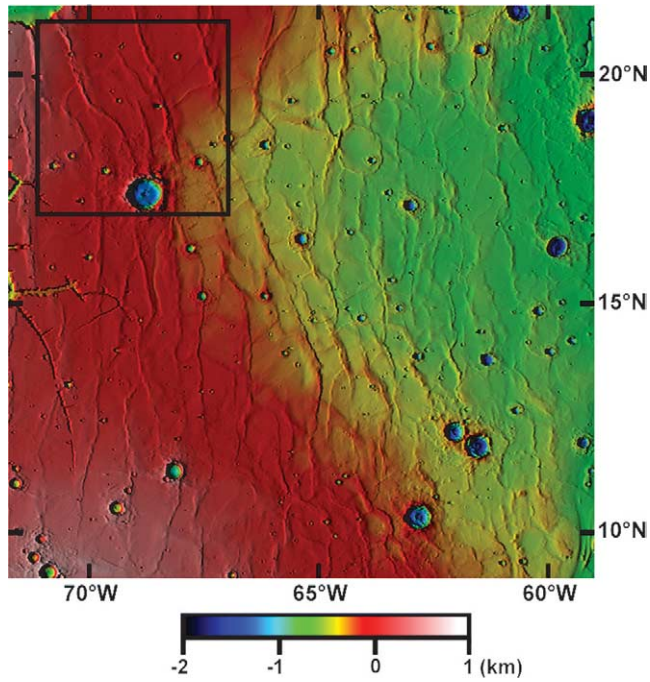

Fig. 1. Color-coded MOLA digital elevation model of northern Lunae Planum overlaid on shaded relief. The ridged plains of Lunae Planum slope downward to the east and are bounded to the north by Kasei Valles. The black box indicates the location of the area shown in Fig. 2A. The digital elevation data is from the MOLA gridded 1/64° per pixel resolution model.

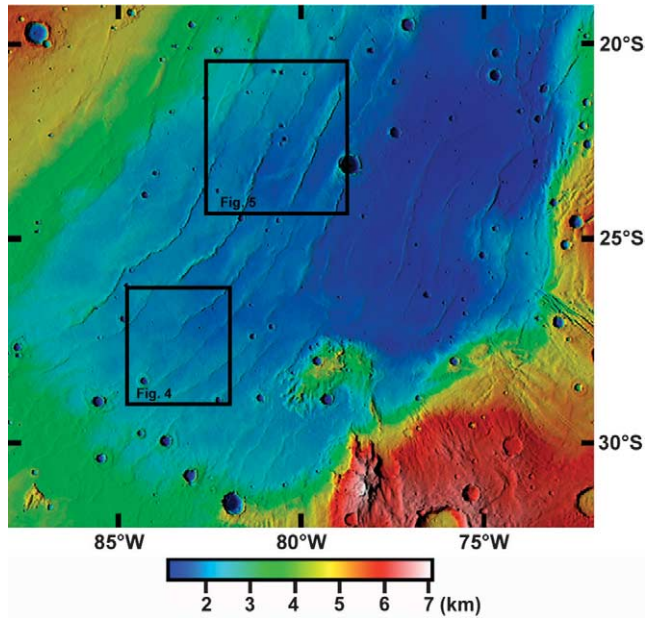

Fig. 3. Color-coded MOLA digital elevation model of Solis Planum overlaid on shaded relief. The ridged plains of Solis Planum occur in a broad valley. The black boxes indicate the locations of the areas shown in Figs. 4A and 5A. The digital elevation data is from the MOLA gridded 1/64° per pixel resolution model.

(~ 12 km) (Fig. 2C). In contrast to LP1, the arch of LP2 increases in elevation away from the ridge in some areas, forming a shallow valley along the structure (east-side of the

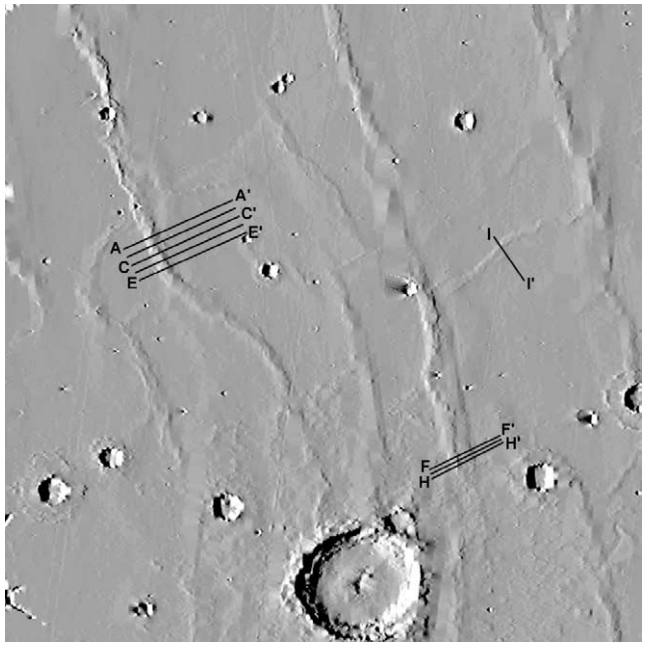

(A)

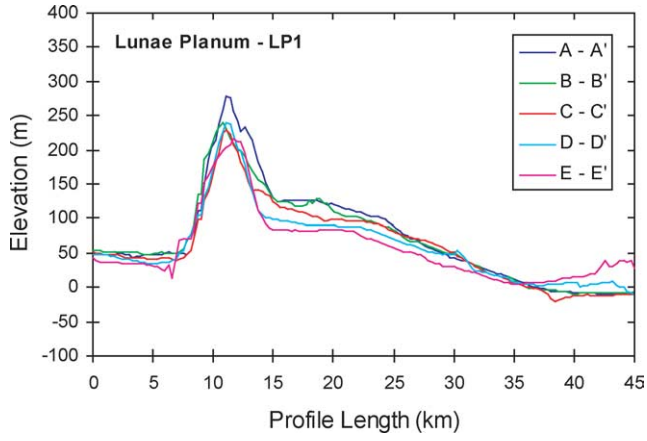

(B)

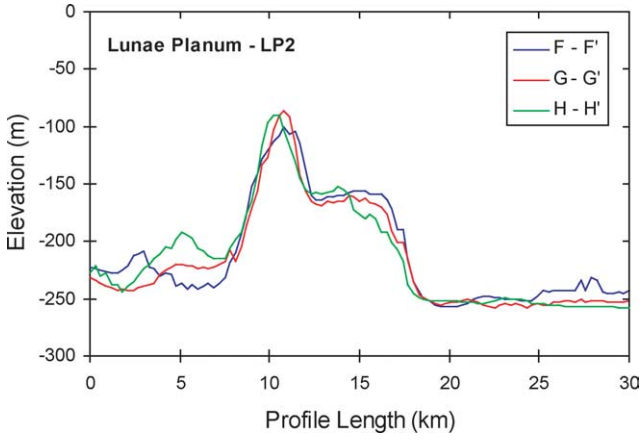

(C)

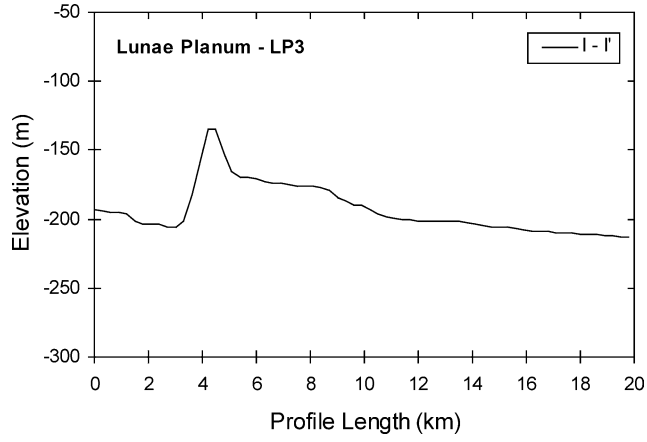

(D)

Fig. 2. (A) Shaded relief image of an area in northern Lunae Planum derived from MOLA data gridded at 300 m/pixel. (B) Profiles across a prominent wrinkle ridge in Lunae Planum (LP1) (vertical exaggeration is ∼ 60 : 1). (C) Profiles across a moderate relief wrinkle ridge segment (LP2) (vertical exaggeration is ∼ 60 : 1). (D) Profile across a small-scale wrinkle ridge cutting across the interridge plains between two regularly spaced ridges (LP3) (vertical exaggeration is ∼ 50 : 1). The locations of the profiles are shown in (A).

ridge) (Fig. 2C). The smallest wrinkle ridge examined in Lunae Planum (LP3) has the same morphologic elements as the two larger structures (Fig. 2D). LP3, however, has about half the relief of LP2 (∼ 70 m) and is only about 8 km wide (Fig. 2D). Unlike LP1 and LP2, this structure has a roughly east–west orientation extending across the interridge plains, intersecting LP2 and another north–northeast trending wrinkle ridge to the east (Figs. 1, 2A). It is important to note that while the three wrinkle ridges are significantly different in scale, they have the same morphology (arch and superimposed ridge) (see Watters, 1988).

2.2. Solis Planum

The ridged plains of southern Solis Planum, in contrast to Lunae Planum, occur in a broad valley bordered on the west by younger flows of Syria Planum and to the east by heavily cratered and faulted highlands (Fig. 3). The wrinkle ridges generally trend north–northeast and are regularly spaced at a distance averaging 30 to 50 km (Watters, 1991) (Fig. 3). Like their counterparts in Lunae Planum, many of the wrinkle ridges in Solis Planum have the same basic morphology. Wrinkle ridge SP1 has a maximum relief of ∼ 100 m and is about 15 km wide (Fig. 4). Unlike the two larger wrinkle ridges studied in Lunae Planum, the vergent side of SP1 is reversed with the ridge located on the opposite flank of the arch (Fig. 4). Changes in vergence are common and may occur on different segments of the same wrinkle ridge (Watters, 1988, 1991). The most prominent wrinkle ridge in Solis Planum (SP2) has a maximum relief of ∼ 320 m and is about 25 km wide (Fig. 5). Its most unusual characteristic, how-

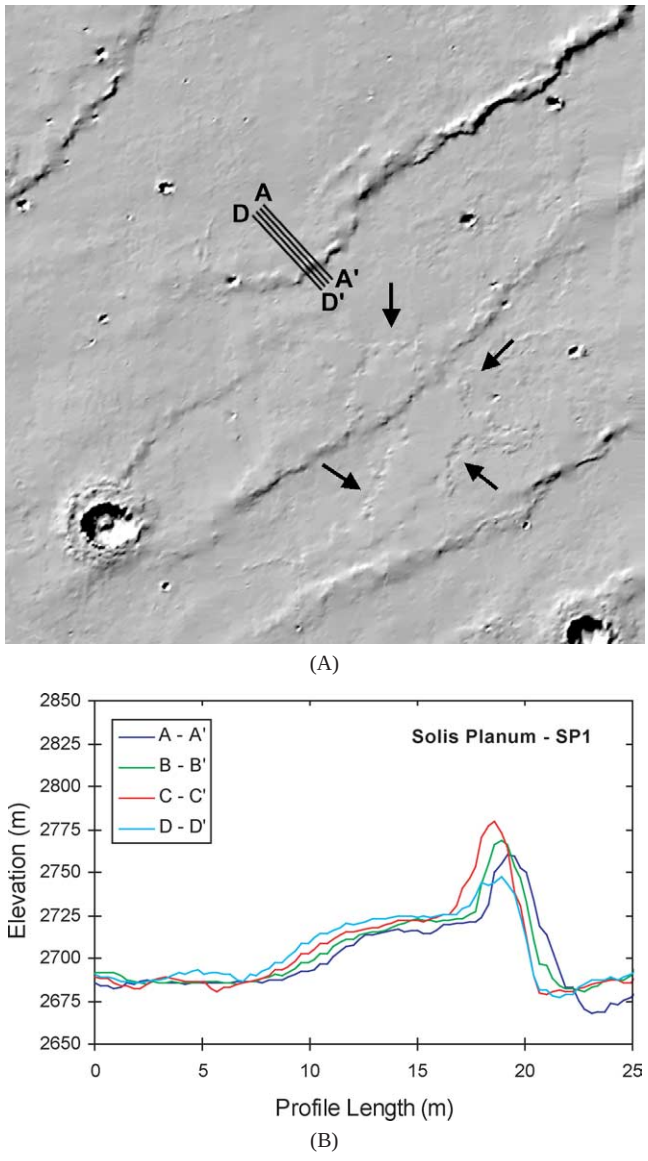

Fig. 4. (A) Shaded relief image of an area in Solis Planum derived from MOLA data gridded at 300 m/pixel. (B) Profiles across a moderate relief wrinkle ridge in Solis Planum (SP1) (vertical exaggeration is ~ 80 : 1). Arrows show the location of a lava flow in the interridge plains that appears to partially cover a wrinkle ridge (see Watters and Maxwell, 1986). The locations of the profiles are shown in (A).

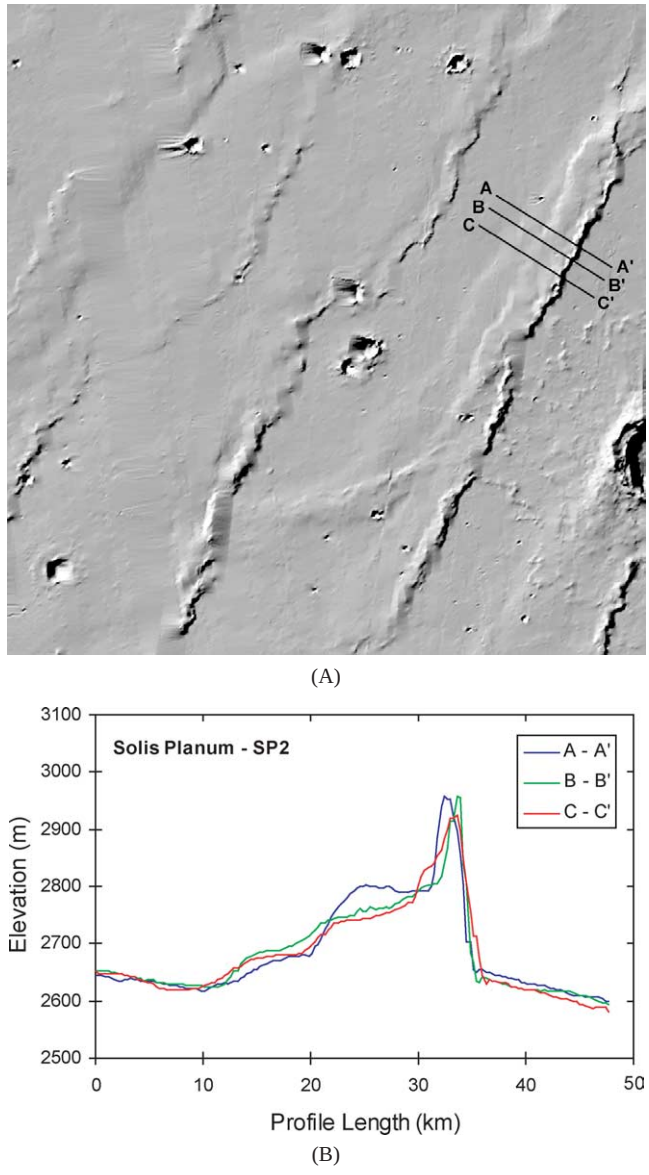

Fig. 5. (A) Shaded relief image of an area in Solis Planum derived from MOLA data gridded at 300 m/pixel. (B) Profiles across a large-scale wrinkle ridge in Solis Planum (SP2) that has a double arch (vertical exaggeration is ~ 50 : 1). The locations of the profiles are shown in (A).

ever, is that the ridge is superimposed on what appears to be a double arch. The ridge is ~ 6 km wide and is superimposed on an upper arch with ~ 120 m of relief that extends ~ 9 km beyond the ridge. The lower arch extends about 19 km from the ridge and has ~ 70 m of relief (Fig. 5). This rare double arch structure may be important in constraining kinematic models for wrinkle ridges.

3. Mechanical modeling

A number of kinematic models have been proposed for wrinkle ridges (see Schultz, 2000, Fig. 2). Fault-bend fold and fault-propagation fold kinematic models have been suggested for wrinkle ridges (Suppe and Narr, 1989; Suppe and Connors, 1992). Although these models can explain the broad uplift or arch, the superimposed ridge cannot be accounted for without introducing additional faults (Schultz, 2000). Multiple-fault kinematic models have been introduced that involve deformation over a blind or surface-breaking thrust fault and the development of a backthrust (Golombek et al., 1991, 2001; Schultz, 2000). The master thrust fault is generally planar and may account for either an elevation offset on the vergent side of the structure or the arch, with the backthrust forming for the ridge (Golombek et al., 1991; Schultz, 2000). Another model involves an array of thrust faults (a primary and two secondary backthrusts)

that intersect in a mechanically weak horizon or décollement (Okubo and Schultz, 2003).

The kinematic model proposed here involves deformation over a single curvilinear or listric thrust fault where the fault flattens into a décollement. The displacement and stresses above a propagating fault is modeled using the elastic dislocation program COULOMB (King et al., 1994; Toda et al., 1998). Elastic dislocation modeling can be used to predict the near-surface topography resulting from slip on a fault. The displacements and stresses are determined for a fault with a specified magnitude and sense of slip using elastic dislocation elements and the stress functions for an elastic half-space (Okada, 1992). This type of modeling has been used to reproduce well understood terrestrial faults (e.g., Stein and King, 1984; King et al., 1988a, 1988b, 1994; King and Ellis, 1990; Bilham and King, 1989; Taboada et al., 1993; Crider and Pollard, 1998). Listric fault geometries have also been modeled using elastic dislocation modeling and the results compared to geodetic and surface scarp height data on terrestrial faults (Ward and Barrientos, 1986; Barrientos et al., 1987; Willsey et al., 2002). Thus, elastic dislocation modeling has been successfully used to model a variety of terrestrial faults with both planar and listric geometries.

The fault surface is defined as a rectangular plane having a fault plane dip and vertical depth of faulting. A listric fault geometry is approximated by linear connecting fault segments with varying dips and lengths. The dips of the fault segments are 30°, 10°, and 5° with a nearly flat (0.01°) final segment. Since there are no obvious surface breaks associated with wrinkle ridges, the thrust faults are assumed to be blind (see Schultz, 2000). The upper tip of the near-surface thrust fault segment is fixed near the edge of the vergent side of the wrinkle ridge (under the ridge) and the lower tip is fixed near the inner edge of the arch, where the fault flattens (Fig. 6). The length L, depth T, and dip θ of the fault segments are free parameters, as is the amount of displacement or slip D on the fault segments. The flat segment (décollement) is assumed to extend for a distance of about 3 times the average ridge spacing. In reality the décollement may be regional in extent, but the predicted horizontal displacements are only significantly influenced if the terminus of the flat segment approaches the maximum width of the wrinkle ridge. In this case, a pronounced syncline is predicted adjacent to the arch that is not observed in the topographic data.

Applying a tapered slip distribution consisting of a small slip on the uppermost segment and equal amounts of slip on the other segments that form the listric geometry (Fig. 6), the major morphologic elements of wrinkle ridges (i.e., the arch and superimposed ridge) are predicted. A tapered slip distribution avoids the unrealistically large stress concentrations near the fault tips that are predicted by uniform slip (Toda et al., 1998). The amount of slip on the fault segments is adjusted until the best fit with the topography is achieved (Fig. 7). Material parameters such as Young's modules and Poisson's ratio of the elastic half-space, and the

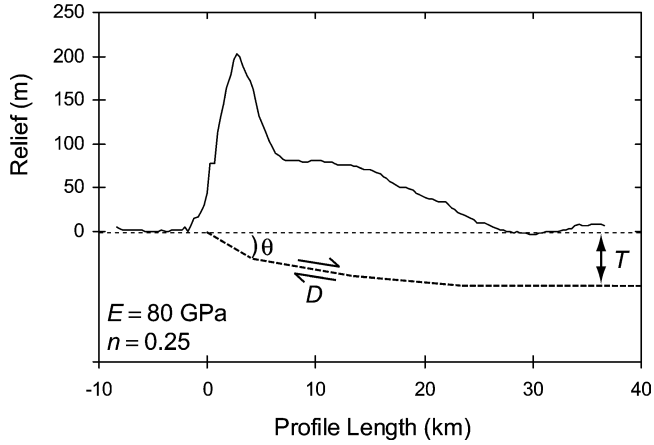

Fig. 6. Detrended topographic profile across the large-scale wrinkle ridge in Lunae Planum (LP1) shown with the listric thrust fault model. The listric geometry is approximated by fault segments with fault-plane dip angles θ of 30°, 10°, and 5° with the final fault segment flattening into a décollement at a maximum depth T. The amount of displacement D or slip on the fault segments is varied until the best fit is achieved. The profile is the mean of 5 profiles across the wrinkle ridge (Fig. 2B). The depth of faulting is not to scale. Vertical exaggeration of topography is ~ 80 : 1.

coefficient of friction of the fault plane are assigned. Initial values for elastic modulus of 80 GPa and Poisson's ratio of 0.25 were used. These values are comparable to those used to model deformation associated with fault offset in terrestrial continental crust (e.g., King et al., 1994; Freed and Lin, 1998).

An analysis of the Coulomb stresses resulting from slip on segments of the listric fault (Fig. 6), assuming a coefficient of friction of 0.4, indicates that large stress concentrations can occur at segment ends, particularly at bends in the fault plane. As expected, the magnitude of the stress is directly related to the amount of the specified slip. Increasing the number of segments that make up the listric fault would be expected to decrease Coulomb stress concentrations at bends in the fault plane. On Earth, secondary fractures often occur where stresses are concentrated along a fault plane, relieving stresses at these locations (King, 1986).

The large-scale wrinkle ridge LP1 was modeled after detrending the mean profile (Fig. 8). The best fit is obtained for a fault with a total slip of ~ 2.2 km (sum of slip on individual fault segments) and a maximum depth (depth to the décollement) of ~ 4.5 km (parameters are shown in Table 1). The same fault geometry was used to model SP2. Varying the amount of slip on the fault segments, a good fit was obtained to the superimposed ridge and the double arch (Fig. 9), with a total of ~ 3.2 km of slip and a maximum depth of faulting of ~ 4.5 km (Table 2). Modeling the smaller wrinkle ridge SP1, the best fit is obtained with a maximum depth of faulting of ~ 2.5 km and a total slip of ~ 0.9 km (Fig. 10, Table 3). This indicates that the variation in scale of wrinkle ridges can be accounted for by listric faults with the same overall geometry but with proportionately smaller fault segments, smaller amounts of slip, and shallower depths of faulting. Thus, the thrust faults associated with small-scale

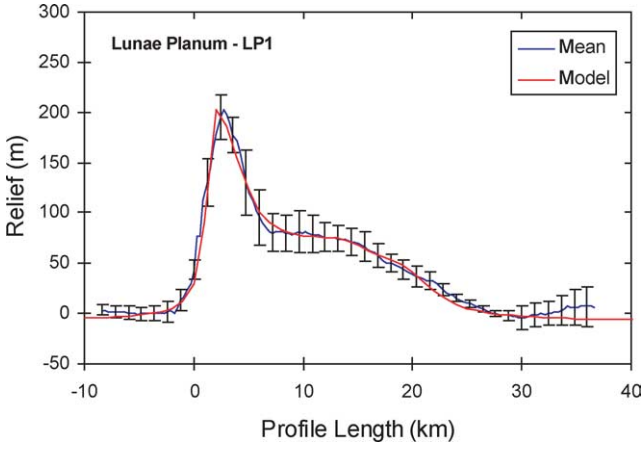

Fig. 7. Cross-section showing a distorted grid resulting from displacements on a listric thrust fault. The initial grid (gray) is in 1 km^2 increments and has a depth of 15 km. The fault (red) has the geometry shown in Fig. 6 and the parameters given in Table 1. The distorted grid (black) shows the expected deformation above and below the listric fault. The vertical exaggeration is $\sim 30:1$.

Table 1
Parameters for the LP1 thrust fault

Segment number	L (km)	$\theta°$	T (km)	D (m)
1	1.92	30	1.0	10.0
2	2.19	30	2.0	350.0
3	5.74	10	3.0	430.0
4	5.74	10	4.0	425.0
5	5.57	5	4.5	450.0
6	85.9	0.01	4.515	500.0

Note. L is the length of the fault segment, θ is the dip of segment, T is the maximum depth of the segment and D is the specified displacement or slip on the segment.

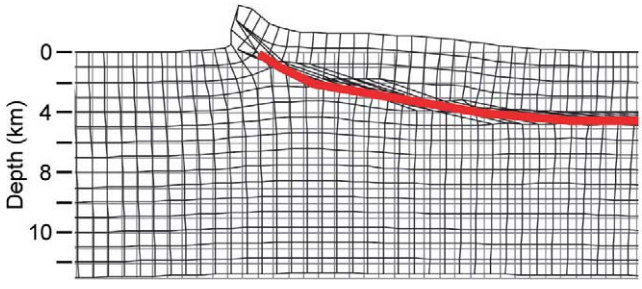

Fig. 8. Comparison of predicted structural relief and detrended topography across a large-scale wrinkle ridge in Lunae Planum (LP1). The topographic profile is the mean of 5 profiles derived from MOLA data gridded at 300 m/pixel with ± 1 standard deviation error bars. The best-fit fault parameters are shown in Table 1. Profile locations are shown in Fig. 2A and the vertical exaggeration is $\sim 90:1$.

wrinkle ridges may be rooted in shallower depth décollements than large-scale wrinkle ridges.

An analysis of the contribution of the uppermost fault segment on the predicted topography shows that for the two large wrinkle ridges modeled (LP1 and SP2), slips of < 10 m have little effect on the relief or morphology. For modeled slips > 10 m, the maximum relief is reduced while the width of the ridge increases. The same trend is found in models of

Table 2
Parameters for the SP2 thrust fault

Segment number	L (km)	$\theta°$	T (km)	D (m)
1	1.92	30	1.0	10.0
2	2.19	30	2.0	545.0
3	5.74	10	3.0	620.0
4	5.74	10	4.0	730.0
5	5.57	5	4.5	620.0
6	85.9	0.01	4.515	700.0

Note. L is the length of the fault segment, θ is the dip of segment, T is the maximum depth of the segment and D is the specified displacement or slip on the segment.

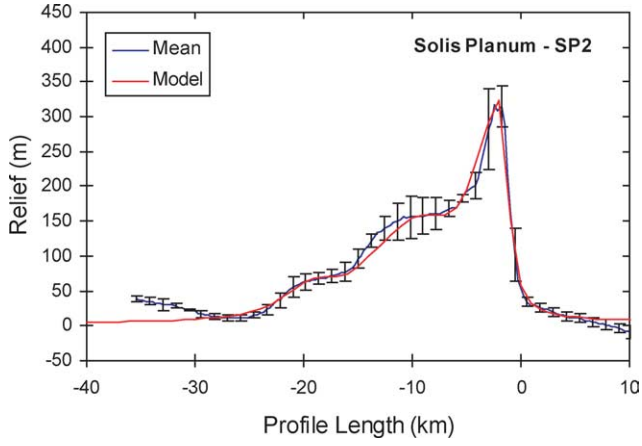

Fig. 9. Comparison of predicted structural relief and topography across a large-scale wrinkle ridge in Solis Planum (SP2). The topographic profile is the mean of 3 profiles derived from MOLA data gridded at 300 m/pixel with ± 1 standard deviation error bars. The best-fit fault parameters are shown in Table 2. Profile locations are shown in Fig. 5A and the vertical exaggeration is $\sim 65:1$.

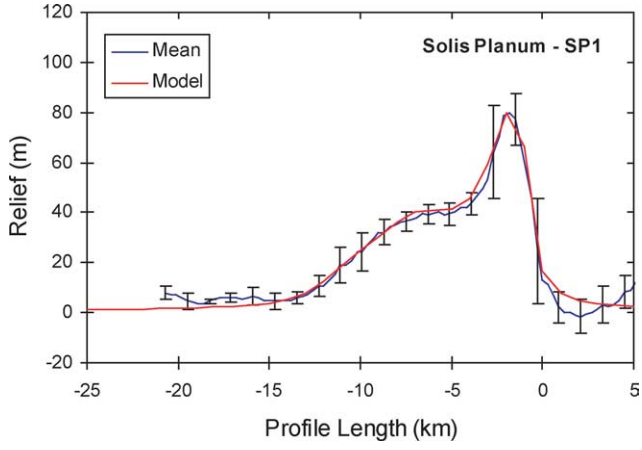

Fig. 10. Comparison of predicted structural relief and topography across a moderate-relief wrinkle ridge in Solis Planum (SP1). The topographic profile is the mean of 4 profiles derived from MOLA data gridded at 300 m/pixel with ± 1 standard deviation error bars. The best-fit fault parameters are shown in Table 3. Profile locations are shown in Fig. 4A and the vertical exaggeration is $\sim 140:1$.

SP1 for slips > 1 m. This indicates that the amount of slip on the uppermost segment of the listric faults must have been relatively small and that slip on the lower segments have the

Table 3
Parameters for the SP1 thrust fault

Segment number	L (km)	$\theta°$	T (km)	D (m)
1	1.23	30	1.0	1.0
2	1.19	30	2.0	120.0
3	2.89	10	3.0	185.0
4	2.84	10	4.0	185.0
5	3.41	5	4.5	210.0
6	85.9	0.01	4.515	220.0

Note. L is the length of the fault segment, θ is the dip of segment, T is the maximum depth of the segment and D is the specified displacement or slip on the segment.

greatest influence on the relief and morphology of wrinkle ridges.

The modeling suggests that the variability in the morphology and dimensions of wrinkle ridges may result from relatively small variations in the cumulative slip on fault segments of listric thrust faults. Variations in the slip distribution along seismically active terrestrial faults are common (e.g., Sieh et al., 1993; Jónsson et al., 2002; Eberhart-Phillips et al., 2003). Slip distributions are often asymmetric or heterogeneous with varying amounts of slip occurring on different sections of the fault (Hernandez et al., 1999; Eberhart-Phillips et al., 2003). Thus, the distribution of slip on the fault segments necessary to best fit the topography of the wrinkle ridges may reflect the accumulation of different amounts of slip on fault segments as the structures developed.

4. Discussion

4.1. Thin-skinned deformation

The mechanical modeling suggests that the thrust faults involved in the larger wrinkle ridges in Solis and Lunae Plana may be rooted in a shallow décollement at a depth of ∼4.5 km. One possibility is that the décollement formed at the contact between ridged plains volcanic material and the underlying megabreccia. Estimates of the thickness of the ridged plains in the Tharsis region vary greatly and are poorly constrained. Thicknesses greater than 0.25 to 1.5 km have been determined using crater depth-diameter relationships (Saunders and Gregory, 1980; DeHon, 1982; Frey et al., 1988). Based on exposed layering in Kasei Valles (see Robinson and Tanaka, 1988), a thickness of the ridged plains of greater than 3.5 km has been suggested (Watters, 1991). Mars Orbiter Camera (MOC) images have revealed evidence layering in the wall material of Valles Marineris (Malin et al., 1998) to depths as great as 8 km (McEwen et al., 1999). The walls of Coprates, Candor, and Ophir Chasmata expose ridged plains material of Lunae Planum and Coprates (Fig. 11). The thickness of layered material exposed in these chasma is estimated to be 4 to 5 km (McEwen et al., 1999). McEwen et al. (1999) interpret the layered material to be volcanic flows based on their morphology, spectral

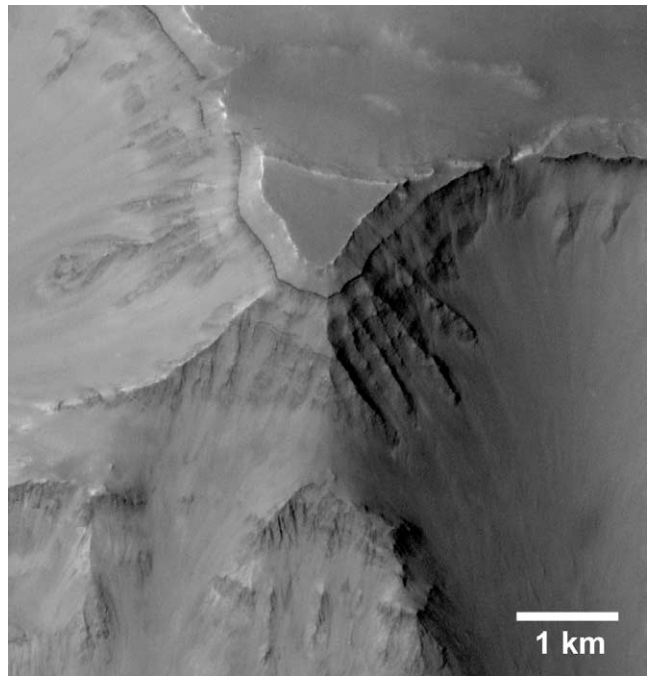

Fig. 11. MOC image of layered ridged plains material exposed in Coprates Catena in Valles Marineris (14.4° S, 55.8° W). The cliffs formed by this sequence are very similar to those formed in terrestrial continental flood basalts like the Columbia River Basalts. The image resolution is ∼5 m/pixel (MOC image # AB1-08003).

properties, and layer thickness, and because the cliffs they form are typical of continental flood basalts. A thickness of the ridged plains in Lunae Planum, Coprates, and adjacent Solis Planum of 4 to 5 km is in good agreement with the modeled maximum depth of faulting of large-scale wrinkle ridges in these provinces. The ridged plains volcanic material is likely to have interbeds separating groups or units of flows (Watters, 1991). This interpretation is supported by MOC images that reveal brighter layers of in situ bedrock within the layered sequences interpreted to be possible intercalated horizons of regolith, pyroclastic volcanic rocks, or sedimentary rocks (Malin et al., 1998). These interbeds are likely to be mechanically weak and may serve to localize shallow décollements. This could be important if, as the modeling suggests, smaller-scale wrinkle ridge thrust faults are rooted in shallow décollements within the ridged plains volcanic sequence. MOC observations of possible interbeds in the ridged plains volcanic material are also significant because of their potential affect on buckling and the initiation of regularly spaced thrust faults (Watters, 1991).

The thin-skinned deformation model is consistent with some terrestrial analogs for wrinkle ridges. On the Columbia Plateau in the northwestern United States, a series of regularly spaced anticlinal ridges are the surface expression of folding and thrust faulting of the Miocene Columbia River Basalts (Watters, 1988, 1989). In addition to forming in flood basalts, the anticlinal ridges are asymmetric in cross section, and changes in vergence are common (Reidel, 1984). The anticlines, like wrinkle ridges, are separated by broad, flat

synclines that are largely undeformed (Reidel et al., 1984; Reidel, 1984). Seismic and gravity data indicate that the thrust faults underlying the anticlinal ridges are confined to the basalt sequence (Saltus, 1993; Jarchow et al., 1994). Low-velocity zones adjacent to the anticlines are interpreted to be brecciated fault planes and have estimated dips ranging from 15° to 45° (Lutter et al., 1994). The large impedance contrasts within the Columbia River Basalts, however, make it difficult to determine the exact geometry of the thrust faults (see Lutter et al., 1994; Jarchow et al., 1994).

Other terrestrial analogs to planetary wrinkle ridges may be found in the Rocky Mountain foreland fold and thrust belt in the Northwest Territories, Canada. Anticlines that form the northern Franklin Mountains are interpreted to be the result of listric thrust faults that flatten into a shallow décollement (Aitkin et al., 1982, Map 1453A; Price, 1986; MacLean and Cook, 1999). The listric fault geometry is supported by seismic data across the Norman Range of the Franklin Mountains (Isaac and Lawton, 2003). These anticlines, formed in a Paleozoic–Mesozoic sedimentary sequence, result from relatively small displacements on the thrust faults and, like wrinkle ridges, are separated by broad flat-bottomed synclines (Aitkin et al., 1982; Price, 1986). Reversals in vergence of the Franklin Mountains structures are also common (Aitkin et al., 1982) and are thought to be facilitated by the presence of a highly ductile layer such as salt (MacLean and Cook, 1999).

4.2. Thick-skinned deformation

Kinematic models for wrinkle ridges that involve deeply rooted thrust faults are based on a number of lines of evidence that include the topography of the ridges, regional topography of ridged plains, and ridge spacing (Zuber and Aist, 1990; Tanaka et al., 1991; Zuber, 1995; Golombek et al., 1991, 2001; Montesi and Zuber, 2003a, 2003b). Golombek et al. (2001) describe Solis and Lunae Plana as having a “stair step” topography that reflects a stacked group of west dipping thrust faults that systematically lower the elevation of the ridged plains. They argue that in many cases, the plains between the ridges do not conform to the regional slope, and elevation offsets across individual ridges are maintained to the next ridge in the series. They suggest that the thrust faults that generated the wrinkle ridges also formed the stair step topography, and that this topography is not simply ridges superimposed on preexisting regional slopes. Golombek et al. (2001) conclude that because the elevation offsets are maintained from one ridge to the next that the underlying thrust faults extend to depths of tens of kilometers, possibly cutting the entire seismogenic lithosphere.

Elevation offsets across wrinkle ridges, however, may not be structurally controlled. Apparent offsets may result from the superposition of the ridge topography on a regional slope (Figs. 2B, 2C) (see Watters and Robinson, 2000; Okubo and Schultz, 2001). In addition, reversals in the regional slope of the ridged plains can occur with no corresponding change in vergence of the wrinkle ridges (i.e., inferred fault geometry). There is also the influence of shallow-depth mechanical discontinuities. Many wrinkle ridges on Mars have clearly been affected by buried impact craters. The common occurrence of circular wrinkle ridges indicates that buried craters may often localize the thrust faults. Examples can be found in every ridged plains province on Mars including Solis and Lunae Plana (see Figs. 1, 3), particularly in Hesperia Planum (see Watters, 1993, Fig. 6; Watters and Robinson, 1997, Fig. A8). While there is evidence that buried impact basins hundreds of kilometers in diameter have influenced the formation of deeply rooted lobate scarp thrust faults on Mercury (Watters et al., 2001, 2004), circular wrinkle ridges appear to be localized by shallow buried craters only tens of kilometers in diameter. Mechanical discontinuities on this scale are more likely to influence thin- than thick-skinned deformation.

One of the most striking features of martian wrinkle ridges is their regular spacing (Watters, 1988). The average spacing varies with ridged plains province, but is generally about 30 km (Watters, 1991). The observed ridge spacing can be accounted for with buckling and localization instability models where the lithosphere is free to deform (Zuber and Aist, 1990; Montesi and Zuber, 2003a, 2003b), or a buckling instability where the lithosphere is assumed to be rigid (Watters, 1991). An alternative approach involves modeling the lithosphere as a thermoelastic half-space with ridge spacing controlled by the amount of slip on underlying thrust faults (Dragoni and Piombo, 2003). There are examples, however, where the spacing is complex. Some wrinkle ridges bifurcate along strike forming two parallel trending ridges. Examples of bifurcating wrinkle ridges are found in northern Lunae Planum (Fig. 1). In other cases, two parallel trending wrinkle ridges will abruptly change trend along strike, crosscut one another, and return to parallel trending ridges (Figs. 1, 3). As described above, there are also cases where wrinkle ridges extend across the interridge plains and intersect parallel trending ridges (Figs. 1, 2A). Bifurcating, crisscrossing, and cross-striking wrinkle ridges indicate a complex pattern of deformation and evolution of stresses that are a challenge to both thick- and thin-skinned models.

4.3. Influence of mechanical properties on fault geometry

Listric thrust faults rooted in shallow décollements are common in terrestrial foreland fold and thrust belts that deform sedimentary sequences (e.g., Boyer and Elliott, 1982; Price, 1986; Cook, 1988). Deeply rooted planar thrust faults that cut crystalline basement rocks are also common in the Rocky Mountain foreland fold and thrust belt (Brewer et al., 1980; Gries, 1983; Stone, 1985, 1993). Structures on Mars and Mercury interpreted to be the surface expression of planar thrust faults are lobate scarps, characterized by a relatively steeply sloping scarp face and a gently sloping back scarp (see Watters, 1993, 2003; Watters and Robinson, 1999; Schultz and Watters, 2001; Watters et al., 1998, 2000, 2001,

2002). Lobate scarps, in contrast to wrinkle ridges, involve surface-breaking thrust faults that clearly offset the walls and floors of transected impact craters (Watters, 1993, 2003; Watters and Robinson, 1999; Watters et al., 1998, 2000, 2004). Elastic dislocation modeling suggests that lobate scarp thrust faults are planar and deeply rooted (Schultz and Watters, 2001; Watters et al., 2002).

The geometry of deeply rooted Rocky Mountain foreland thrust faults changes when they propagate from crystalline basement rocks into the overlying Paleozoic sedimentary sequence. Seismic data shows that the geometry of the thrust faults is generally listric in the sediments and planar in the crystalline basement (Stone, 1985, 1993). These data also show secondary listric thrust faults that commonly flatten into bedding planes or interbedded evaporite zones in the sedimentary sequence (Stone, 1993, Fig. 13). The change in fault geometry between the basement and the sediments is attributed to a contrast in mechanical properties (Stone, 1993). Such a contrast in properties may explain the difference in geometry between thrust faults forming lobate scarps and wrinkle ridges (planar versus listric). Martian lobate scarps occur in intercrater plains material in the heavily cratered highlands (Watters, 1993, 2003; Watters and Robinson, 1999). MOC images have revealed evidence of widespread layering in the intercrater plains (Malin et al., 1998; Malin and Edgett, 2000). Although the composition (and thickness) of the intercrater plains layered sequence is not well constrained, it may consist of sedimentary or volcanic deposits (Malin and Edgett, 2000) overlying a thick megabreccia. Thus, the presence or absence of layering by itself may not produce the necessary contrast in the mechanical properties.

The strength of a multilayer is determined by the mechanical nature of the contacts between the layers (Johnson, 1980). It has been shown that a blind thrust fault propagating upward will induce folding of a multilayer if the layer contacts are weak (i.e., low shear strength) (Nino et al., 1998). Conversely, if the contacts are strong, faulting is favored and the fault is expected to propagate through the sequence and become surface-breaking (Roering et al., 1997; Nino et al., 1998). The fact that lobate scarps form over surface-breaking thrust faults suggests that the layer contacts in intercrater plains are strong and resist slip. Slip between layers (or groups of layers) in the ridged plains probably occurred in interbeds with low shear strengths (Watters, 1991). These interbeds may account for the contrast in mechanical properties between intercrater plains and ridged plains that promote the formation of a listric fault geometry, and facilitate flexural slip folding that inhibits blind thrust faults from propagating to the surface (see Schultz, 2000).

5. Conclusions

Mechanical modeling of wrinkle ridges suggests that the two major morphologic features of these structures (i.e., broad arch and superimposed ridge) can be approximated by a single thrust fault with a listric geometry. The modeling suggests that the thrust faults are rooted in décollements that may vary in depth with the scale of the wrinkle ridge. In the case of large-scale wrinkle ridges, the décollement may correspond to the contact between the ridged plains volcanic sequence and the megaregolith or megabreccia. The thrust faults involved with smaller-scale wrinkle ridges may be rooted in shallow interbeds in the ridged plains volcanic sequence. However, with topographic data alone to constrain elastic dislocation modeling, a unique interpretation of the fault geometry and maximum depth of faulting is not possible. The results of this study are thus intended to introduce another plausible model of the origin of wrinkle ridges; one involving thin-skinned deformation of upper crustal materials. New insight into the shallow crustal structure of Mars will be obtained in the near future from radar sounders. With data from the Mars Advanced Radar for Subsurface and Ionospheric Sounding (MARSIS) instrument on the Mars Express Mission, it may be possible to resolve thrust faults in ridged plains material to depths of 3 to 5 km and test models for the origin of wrinkle ridges.

Acknowledgments

I thank W. Bruce Banerdt and an anonymous reviewer for their reviews and constructive comments. I also thank Ross S. Stein for his review of an earlier manuscript and helpful discussions on the use of COULOMB, and to Richard A. Schultz for many valuable discussions on wrinkle ridges. This research was supported by a grant from National Aeronautics and Space Administration's Mars Data Analysis Program.

References

Aitkin, J.D., Cook, D.G., Yorath, C.J., 1982. Upper Ramparts River (106G) and Sans Sault Rapids (106H) map areas, District of Mackenzie. Geol. Sur. Canada, Mem. 388, 1–48.

Barrientos, S.E., Stein, R.S., Ward, S.N., 1987. Comparison of the 1959 Hebgen Lake, Montana, and the 1983 Borah Peak, Idaho, earthquakes from geodetic observations. Bull. Seismol. Soc. Am. 77, 784–808.

Bilham, R., King, G., 1989. The morphology of strike-slip faults: examples from the San Andreas Fault, California. J. Geophys. Res. 94, 10204–10216.

Boyer, S.E., Elliott, D., 1982. Thrust systems. Am. Assoc. Petrol. Geol. Bull. 66, 1196–1230.

Brewer, J.A., Smithson, S.B., Oliver, J.E., Kaufman, S., Brown, L.D., 1980. The Laramide orogeny: evidence form COCORP deep crustal seismic profiles in the Wind River mountains, Wyoming. Tectonophysics 62, 165–189.

Bryan, W.B., 1973. Wrinkle-ridges as deformed surface crust on ponded mare lava. Geochim. Cosmochim. Acta Suppl. 1, 93–106.

Cook, F.A., 1988. Proterozoic thin-skinned thrust and fold belt beneath the Interior Platform in northwestern Canada. Geol. Soc. Am. Bull. 100, 877–890.

Crider, J.G., Pollard, D.D., 1998. Fault linkage: 3-D mechanical interaction between normal faults. J. Geophys. Res. 103, 24373–24391.

DeHon, R.A., 1982. Martian volcanic materials: preliminary thickness estimates in the eastern Tharsis region. J. Geophys. Res. 87, 9821–9828.

Dragoni, M., Piombo, A., 2003. A model for the formation of wrinkle ridges in volcanic plains on Venus. Phys. Earth Planet. Int. 135, 161–171.

Eberhart-Phillips, D., 28 colleagues, 2003. The 2002 Denali fault earthquake, Alaska: a large magnitude, slip-partitioned event. Science 300, 1113–1118.

Freed, A.M., Lin, J., 1998. Time-dependent changes in failure stress following thrust earthquakes. J. Geophys. Res. 103, 24393–24409.

Frey, H., Semeniuk, J., Grant, T., 1988. Early resurfacing events on Mars (abstract). In: MEVTV Workshop: Early Tectonic and Volcanic Evolution of Mars. Lunar and Planetary Institute, Houston, TX, pp. 24–26.

Golombek, M.P., Plescia, J.B., Franklin, B.J., 1991. Faulting and folding in the formation of planetary wrinkle ridges. In: Proc. Lunar Planet. Sci. Conf. 21st, pp. 679–693.

Golombek, M.P., Anderson, F.S., Zuber, M.T., 2001. Martian wrinkle ridge topography: evidence for subsurface faults from MOLA. J. Geophys. Res. 106, 23811–23821.

Gries, R., 1983. Oil and gas prospecting beneath Precambrian of foreland thrust plates in Rocky Mountains. Am. Assoc. Petrol. Geol. Bull. 67, 1–28.

Hernandez, B., Cotton, F., Campillo, M., 1999. Contribution of radar interferometry to a two-step inversion of the kinematic process of the 1992 Landers earthquake. J. Geophys. Res. 104, 13083–13099.

Howard, K.A., Muehlberger, W.R., 1973. Lunar thrust faults in the Taurus–Littrow region. In: Apollo 17 Preliminary Science Report. NASA SP, vol. 330, pp. 31-32–31-25.

Isaac, J.H., Lawton, D.C., 2003. Benefits of integrated seismic and gravity exploration: an example form Norman Wells, NWT. In: CSEG/CSPG Ann. Meeting. Expanded abstract.

Jarchow, C.M., Catchings, R.D., Lutter, W.J., 1994. Large-explosion source, wide-recording aperture, seismic profiling on the Columbia Plateau, Washington. Geophysics 59, 259–271.

Johnson, A.M., 1980. Folding and faulting of strain-hardening sedimentary rocks. Tectonophysics 62, 251–278.

Jónsson, S., Zebker, H., Segall, P., Amelung, F., 2002. Fault slip distribution of the 1999 Mw 7.1 Hector Mine, California, earthquake, estimated from satellite radar and GPS measurements. Bull. Seismol. Soc. Am. 92, 1377–1389.

King, G.C.P., 1986. Speculations on the geometry of the initiation and termination processes of earthquake rupture and its relation to morphology and geological structure. Pure Appl. Geophys. 124, 567–585.

King, G.C.P., Ellis, M., 1990. The origin of large local uplift in extensional regions. Nature 348, 20–27.

King, G.C.P., Stein, R.S., Rundle, J.B., 1988a. The growth of geological structures by repeated earthquakes. 1. Conceptual framework. J. Geophys. Res. 93, 13307–13318.

King, G.C.P., Stein, R., Rundle, J.B., 1988b. The growth of geological structures by repeated earthquakes. 2. Field examples of continental dip-slip faults. J. Geophys. Res. 93, 13319–13331.

King, G.C.P., Stein, R.S., Lin, J., 1994. Static stress changes and the triggering of earthquakes. Bull. Seismol. Soc. Am. 84, 935–953.

Lucchitta, B.K., 1976. Mare ridges and related highland scarps—results of vertical tectonism. Geochim. Cosmochim. Acta Suppl. 3, 2761–2782.

Lucchitta, B.K., 1977. Topography, structure, and mare ridges in southern Mare Imbrium and northern Oceanus Procellarum. Geochim. Cosmochim. Acta Suppl. 3, 2691–2703.

Lutter, W.J., Catching, R.D., Jarchow, C.M., 1994. An image of the Columbia Plateau form inversion of high-resolution seismic data. Geophysics 59, 1278–1289.

MacLean, B.C., Cook, D.G., 1999. Salt tectonism in the Fort Norman area, Northwest Territories, Canada. Bull. Can. Petrol. Geol. 47, 104–135.

Malin, M.C., Edgett, K.S., 2000. Sedimentary rocks of early Mars. Science 290, 1927–1937.

Malin, M.C., 15 colleagues, 1998. Early views of the martian surface from the Mars Orbiter Camera of Mars Global Surveyor. Science 279, 1681–1685.

Maxwell, T.A., Phillips, R.J., 1978. Stratigraphic correlation of the radar detected subsurface interface in Mare Crisium. Geophys. Res. Lett. 5, 811–814.

Maxwell, T.A., El-Baz, F., Ward, S.W., 1975. Distribution, morphology, and origin of ridges and arches in Mare Serenitatis. Geol. Soc. Am. Bull. 86, 1273–1278.

McEwen, A.S., Malin, M.C., Carr, M.H., Hartmann, W.K., 1999. Voluminous volcanism on early Mars revealed in Valles Marineris. Nature 397, 584–586.

Montesi, L.G.J., Zuber, M.T., 2003a. Spacing of faults at the scale of the lithosphere and localization instability: 1. Theory. J. Geophys. Res. 108, 2110.

Montesi, L.G.J., Zuber, M.T., 2003b. Clues to the lithospheric structure of Mars from wrinkle ridge sets and localization instablility. J. Geophys. Res. 108, 5048.

Muehlberger, W.R., 1974. Structural history of southeastern Mare Serenitatis and adjacent highlands. Geochim. Cosmochim. Acta Suppl. 1, 101–110.

Nino, P., Philip, H., Chery, J., 1998. The role of bed-parallel slip in the formation of blind thrust faults. J. Struct. Geol. 20, 503–516.

Neumann, G.A., Rowlands, D.D., Lemoine, F.G., Smith, D.E., Zuber, M.T., 2001. Crossover analysis of Mars Orbiter Laser Altimeter data. J. Geophys. Res. 106, 23753–23768.

Okada, Y., 1992. Internal deformation due to shear and tensile faults in a half-space. Bull. Seismol. Soc. Am. 82, 1018–1040.

Okubo, C.H., Schultz, R.A., 2001. Elevation offsets across wrinkle ridges: Key to structural width. In: Proc. Lunar Planet. Sci. Conf. 32nd. Lunar and Planetary Institute, Houston, TX. Abstract #2086 [CD-ROM].

Okubo, C.H., Schultz, R.A., 2003. Two-dimensional wrinkle ridge strain & energy release based on numerical modeling of MOLA topography. In: Proc. Lunar Planet. Sci. Conf. 34th. Lunar and Planetary Institute, Houston, TX. Abstract #1286 [CD-ROM].

Plescia, J.B., 1991. Wrinkle ridges in Lunae Planum, Mars: implications for shortening and strain. Geophys. Res. Lett. 18, 913–916.

Plescia, J.B., 1993. Wrinkle ridges of Arcadia Planitia, Mars. J. Geophys. Res. 98, 15049–15059.

Plescia, J.B., Golombek, M.P., 1986. Origin of planetary wrinkle ridges based on the study of terrestrial analogs. Geol. Soc. Am. Bull. 97, 1289–1299.

Price, R.A., 1986. The southeastern Canadian Cordillera: thrust faulting, tectonic wedging, and delamination of the lithosphere. J. Struct. Geol. 8, 239–254.

Reidel, S.P., 1984. The Saddle Mountains: the evolution of an anticline in the Yakima fold belt. Am. J. Sci. 284, 942–978.

Reidel, S.P., Scott, G.R., Bazard, D.R., Cross, R.W., Dick, B., 1984. Post-12 million year clockwise rotation in the central Columbia Plateau, Washington. Tectonics 3, 251–273.

Robinson, M.S., Tanaka, K.L., 1988. Stratigraphy of the Kasei Valles region. In: MEVTV Workshop: Nature and Composition of Surface Units on Mars. Lunar and Planetary Institute, Houston, TX, pp. 106–108. Abstract.

Roering, J.J., Cooke, M.L., Pollard, D.D., 1997. Why blind thrust faults do not propagate to the Earth's surface: numerical modeling of coseismic deformation associated with thrust-related anticlines. J. Geophys. Res. 102, 12901–12912.

Saltus, R.W., 1993. Upper crustal structure beneath the Columbia River Basalt Group, Washington: gravity interpretation controlled by borehole and seismic studies. Geol. Soc. Am. Bull. 105, 1247–1259.

Saunders, R.S., Gregory, T.E., 1980. Tectonic implications of martian ridged plains. In: Reports of Planetary Geology Program, 1980, NASA Tech. Memo. TM82385, pp. 93–94. Abstract.

Schultz, R.A., 2000. Localization of bedding-plane slip and backthrust faults above blind thrust faults: keys to wrinkle ridge structure. J. Geophys. Res. 105, 12035–12052.

Schultz, R.A., Watters, T.R., 2001. Forward mechanical modeling of the Amenthes Rupes thrust fault on Mars. Geophys. Res. Lett. 28, 4659–4662.

Sieh, K., Jones, L., Hauksson, E., Hudnut, K., Eberhart-Phillips, D., Heaton, T., Hough, S., Hutton, K., Kanamori, H., Lilje, A., Lindvall, S., McGill, S.F., Mori, J., Rubin, C., Spotila, J.A., Stock, J., Thio, H.K., Treiman, J., Wernicke, B., Zachariasen, J., 1993. Near-field investigations of the Landers earthquake sequence, April to July 1992. Science 260, 171–176.

Sharpton, V.L., Head, J.W., 1982. Stratigraphy and structural evolution of southern Mare Serenitatis: a reinterpretation based on Apollo Lunar Sounder Experiment data. J. Geophys. Res. 87, 10983–10998.

Sharpton, V.L., Head, J.W., 1988. Lunar mare ridges: analysis of ridge-crater intersections and implications for the tectonic origin of mare ridges. In: Proc. Lunar Planet. Sci. Conf. 18th, pp. 307–317.

Smith, D.E., 11 colleagues, 1998. Topography of the northern hemisphere of Mars from the Mars Orbiter Laser Altimeter. Science 279, 1686–1692.

Smith, D.E., 18 colleagues, 1999. The global topography of Mars and implications for surface evolution. Science 279, 1495–1503.

Smith, D.E., et al., 2001. Mars Orbiter Laser Altimeter: experiment summary after the first year of global mapping of Mars. J. Geophys. Res. 106, 23689–23722.

Stein, R.S., King, G.C.P., 1984. Seismic potential revealed by surface folding: the 1983 Coalinga, California, earthquake. Science 224, 869–872.

Stone, D.S., 1985. Geologic interpretation of seismic profiles, Big Horn Basin, Wyoming, Part I. East flank. In: Gries, R.R., Dyer, R.C. (Eds.), Seismic Exploration of the Rocky Mountain Region. Rocky Mountain Association of Geologists, pp. 165–174.

Stone, D.S., 1993. Basement-involved thrust-generated folds as seismically imaged in the subsurface of the central Rocky Mountain foreland. In: Schmidt, D.J., Chase, R.B., Erslev, E.A. (Eds.), Laramide Basement Deformation in the Rocky Mountain Foreland of the Western United States. Spec. Pap. Geol. Soc. Am., vol. 280, pp. 271–318.

Strom, R.G., 1972. Lunar mare ridges, rings and volcanic ring complexes. Mod. Geol. 2, 133–157.

Suppe, J., Connors, C., 1992. Critical taper wedge mechanics of fold-and thrust belts on Venus: initial results from Magellan. J. Geophys. Res. 97, 13545–13561.

Suppe, J., Narr, W., 1989. Fault-related folding on the Earth with application to wrinkle ridges on Mars and the Moon. In: MEVTV Workshop on Tectonic Features on Mars. Lunar and Planetary Institute, Houston, TX, pp. 29–30. Abstract.

Taboada, A., Bousquet, J.C., Philip, H., 1993. Coseismic elastic models of folds above blind thrusts in the Betic Cordilleras (Spain) and evaluation of seismic hazard. Tectonophysics 220, 223–241.

Tanaka, K.L., Golombek, M.P., Banerdt, W.B., 1991. Reconciliation of stress and structural histories of the Tharsis region of Mars. J. Geophys. Res. 96, 15617–15633.

Toda, S., Stein, R.S., Reasenberg, P.A., Dieterich, J.H., Yoshida, A., 1998. Stress transferred by the 1995 Mw = 6.9 Kobe, Japan, shock: effect on aftershocks and future earthquake probabilities. J. Geophys. Res. 103, 24543–24565.

Ward, S.N., Barrientos, S.E., 1986. An Inversion for Slip Distribution and Fault Shape from Geodetic Observations of the 1983 Borah Peak, Idaho, Earthquake. J. Geophys. Res. 91, 4909–4919.

Watters, T.R., 1988. Wrinkle ridge assemblages on the terrestrial planets. J. Geophys. Res. 93, 10236–10254.

Watters, T.R., 1989. Periodically spaced anticlines of the Columbia Plateau. In: Reidel, S.P., Hooper, P.R. (Eds.), Volcanism and Tectonism in the Columbia River Flood-Basalt Province. Spec. Pap. Geol. Soc. Am., vol. 238, pp. 283–292.

Watters, T.R., 1991. Origin of periodically spaced wrinkle ridges on the Tharsis plateau of Mars. J. Geophys. Res. 96, 15599–15616.

Watters, T.R., 1993. Compressional tectonism on Mars. J. Geophys. Res. 98, 17049–17060.

Watters, T.R., 2001. Studies of martian wrinkle ridges using MOLA topographic data: the nature of elevation offsets. In: Proc. Lunar Planet. Sci. Conf. 32nd. Lunar and Planetary Institute, Houston, TX. Abstract #1414 [CD-ROM].

Watters, T.R., 2003. Thrust faulting along the dichotomy boundary in the eastern hemisphere of Mars. J. Geophys. Res. 108. 8-1–8-12.

Watters, T.R., Maxwell, T.A., 1986. Orientation, relative age, and extent of the Tharsis Plateau ridge system. J. Geophys. Res. 91, 8113–8125.

Watters, T.R., Robinson, M.S., 1997. Radar and photoclinometric studies of wrinkle ridges on Mars. J. Geophys. Res. 102, 10889–10903.

Watters, T.R., Robinson, M.S., 1999. Lobate Scarps and the origin of the martian crustal dichotomy. J. Geophys. Res. 104, 18981–18990.

Watters, T.R., Robinson, M.S., 2000. Topographic studies of wrinkle ridges: the significance of elevation offsets. In: Proc. Lunar Planet. Sci. Conf. 31st. Lunar and Planetary Institute, Houston, TX. Abstract #1879 [CD-ROM].

Watters, T.R., Robinson, M.S., Cook, A.C., 1998. Topography of lobate scarps on Mercury: new constraints on the planet's contraction. Geology 26, 991–994.

Watters, T.R., Robinson, M.S., Cook, A.C., 2001. Large-scale lobate scarps in the southern hemisphere of Mercury. Planet. Space Sci. 49, 1523–1530.

Watters, T.R., Schultz, R.A., Robinson, M.S., 2000. Displacement-length relations of thrust faults associated with lobate scarps on mercury and Mars: comparison with terrestrial faults. Geophys. Res. Lett. 27, 3659–3662.

Watters, T.R., Schultz, R.A., Robinson, M.S., Cook, A.C., 2002. The mechanical and thermal structure of Mercury's early crust. Geophys. Res. Lett. 29. 37-1–37-4.

Watters, T.R., Robinson, M.S., Bina, C.R., Spudis, P.D., 2004. Thrust faults and the global contraction Mercury. Geophys. Res. Lett. 31. L04701.

Willsey, S.P., Umhoefer, P.J., Hilley, G.E., 2002. Early evolution of an extensional monocline by a propagating normal fault: 3D analysis form combined field study and numerical modeling. J. Struct. Geol. 24, 651–669.

Zuber, M.T., 1995. Wrinkle ridges, reverse faulting, and the depth penetration of lithospheric strain in Lunae Planum, Mars. Icarus 114, 80–92.

Zuber, M.T., Aist, L.L., 1990. The shallow structure of the martian lithosphere in the vicinity of the ridged plains. J. Geophys. Res. 95, 14215–14230.

Zuber, M.T., Smith, D.E., Solomon, S.C., Muhleman, D.O., Head, J.W., Garvin, J.B., Abshire, J.B., Bufton, J.L., 1992. The Mars Observer Laser Altimeter investigation. J. Geophys. Res. 97, 7781–7797.

Zuber, M.T., 14 colleagues, 2000. Internal structure and early thermal evolution of Mars from Mars Global Surveyor topography and gravity. Science 287, 1788–1793.